



pubs.acs.org/JPCB Article

Quantum Simulations of Hydrogen Bonding Effects in Glycerol Carbonate Electrolyte Solutions

Published as part of The Journal of Physical Chemistry virtual special issue "Lawrence R. Pratt Festschrift".

Andrew E. Eisenhart* and Thomas L. Beck*



Cite This: https://dx.doi.org/10.1021/acs.jpcb.0c10942



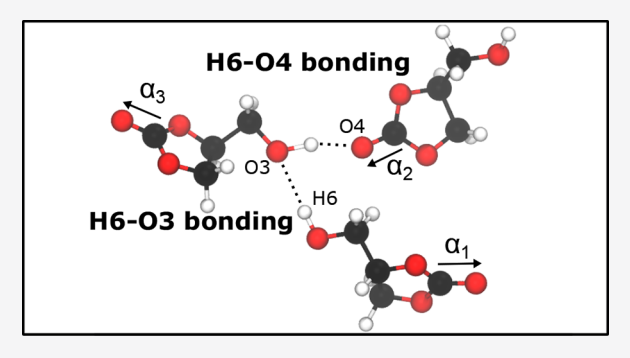
ACCESS

III Metrics & More

Article Recommendations

Supporting Information

ABSTRACT: The need for environmentally friendly nonaqueous solvents in electrochemistry and other fields has motivated recent research into the molecular-level solvation structure, thermodynamics, and dynamics of candidate organic liquids. In this paper, we present the results of quantum density functional theory simulations of glycerol carbonate (GC), a molecule that has been proposed as a solvent for green industrial chemistry, nonaqueous alternatives for biocatalytic reactions, and liquid media in energy storage devices. We investigate the structure and dynamics of both the pure GC liquid and electrolyte solutions containing KF and KCl ion pairs. These simulations reveal the importance of hydrogen bonding that controls the structural and dynamic behavior of the pure liquid and ion association in the



electrolyte solutions. The results illustrate the difficulties associated with classical modeling of complex organic solvents. The simulations lead to a better understanding of the underlying mechanisms behind the previously observed peculiar ion-specific behavior in GC electrolyte solutions.

1. INTRODUCTION

Linear and cyclic carbonate molecules have been the subject of recent extensive study due to their utility as solvents in a variety of chemical systems. One of the primary applications has been their key role as liquid media for electrolytes in lithium-ion batteries. The cyclic carbonate molecules ethylene and propylene carbonate (EC, PC) share features that make them ideal for solvating ions in solution, high polarizabilities, and resulting large dielectric constants. In high polarizabilities, and resulting large dielectric constants. As an indicator of the impact of the addition of a single methyl group in PC relative to EC, the PC solid displays a melting temperature 90.9 C below that for EC (38.2 °C).

A third member of this series, glycerol carbonate, (4-hydroxymethyl-1,3-dioxolan-2-one or GC, see Figure 1) results from the conversion of one H atom on the methyl group of PC to an OH hydroxyl group. Developments in the world of green chemistry have identified GC as a potentially diverse chemical building block due to its wide reactivity ^{11–16} and its role in the valorization of biofuel manufacturing byproducts, specifically glycerol. ^{17,18} These applications come in addition to potential uses in energy storage devices ¹⁷ and as a novel nonaqueous solvent for biocatalysis. ¹⁹

GC exhibits a large dipole moment (5.05 D⁸) as seen in EC and PC. The hydroxyl tail, however, leads to hydrogen bonding possibilities in the liquid. Those hydrogen bonds in GC can be between OH groups and/or between the OH group and the

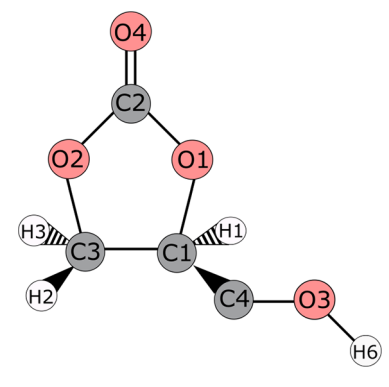


Figure 1. Glycerol carbonate labeling convention used in this paper.

carbonyl oxygen. Further, the OH group can form hydrogen bonds to dissolved anions. Interestingly, while the EC and GC liquids are completely miscible with water, the PC/water mixture exhibits liquid–liquid phase separation.²⁰ Thus, the

Received: December 7, 2020 Revised: January 28, 2021



EC/PC/GC sequence provides a fascinating and challenging testing ground for molecular theory. In addition, by comparing and contrasting specific ion solvation in these liquids with that in water, insights can be gained into a broader range of ion solvation environments that have implications for biological solutions.²¹

In the bulk phase, GC exhibits a high viscosity of 85.4 cP at 25 °C (compared to EC at 1.90 cP, PC at 2.53 cP, and water at 0.89 cP) and yet displays a melting point of -70.8 °C, which is lower than that of PC (-52.7 °C) and much below EC. 10,17 The GC liquid temperature range is remarkably large, 425 °C, since the boiling temperature is significantly higher than for EC and PC. Clearly, hydrogen bonding interactions are heavily involved in producing these unique liquid properties.

The structure and dynamics of the GC liquid can be impacted by the addition of certain salt pairs to the solution. 10,22 KF, as an example, substantially increases the glass transition temperature from -70.8 °C for pure GC to -61.3 °C for the electrolyte solution. The KCl ion pair, on the other hand, has little effect on the transition temperature.

A recent study²³ has compared the liquid structure of GC to PC using neutron scattering and molecular modeling techniques. The modeling utilized a molecular force field involving Lennard-Jones and point charge interactions which were fit to the scattering data using an iterative process and Monte Carlo simulations. Those simulations were then used to infer structural details not included in the total structure factor. Other simulation methods employed in modeling aqueous and organic liquids have utilized polarizable force fields fit to ab initio quantum chemistry calculations and experimental data.²⁴⁻²⁶ Additional classical models have incorporated scaled atomic partial charges to mimic electronic polarization effects.²⁷ Those models produced relatively accurate results for the transfer free energy of the Li⁺ ion between water and the organic phase and for the ion diffusion constants. This same approach, however, encounters difficulties in reproducing the experimental enthalpies and free energies of molecular solvation in room temperature ionic liquids.²⁸ Inclusion of explicit polarization improves both the agreement with experiment and the transferability of the force fields.

In previous work, we first explored ion solvation thermodynamics in EC and PC using classical force field models.²⁹ The simulations showed that although relatively accurate solvation free energies could be obtained the computed solvation enthalpies and entropies deviated significantly from experiment. Subsequent quantum simulations revealed the origin of the computed discrepancies as due to significant solvent molecular polarization in the strong field of the ion. In this study, we present results related to the structure and dynamics of pure GC and electrolyte solutions using ab initio molecular dynamics (AIMD) simulations for comparison with classical models. In particular, we examine in detail the impact of hydrogen bonding and the importance of accurate quantum modeling in these systems. The purpose of the simulations is to gain a basic understanding of the key interactions that drive the observed complex behavior of the GC solutions. Other recent quantum simulations of EC and PC solutions have explored structure and dynamics in these liquids. 30,31

The remainder of the paper is organized as follows. We first discuss the computational methods employed in our classical and quantum simulations and charge transfer calculations. We then present the results of the calculations with associated discussion. Finally, we summarize the conclusions of our work.

METHODS

Molecular Dynamics. The classical molecular dynamics (MD) simulations were performed using the GROMACS³² suite of codes (v2020.2). The OPLS-AA general force field was employed to model the GC molecules. The parameters were obtained from the LigParGen online utility. $^{33\hat{-}35}$ The Particle-Mesh Ewald (PME) method was used to model the long-range electrostatic interactions, and long-range energy and pressure corrections were applied to the Lennard-Jones interactions for systems with a side length less than 2 nm.³⁶ Three systems were created for the present study: one unit cell containing 32 GC molecules, and two electrolyte systems containing one ion pair each of either KF or KCl solvated with 27 GC molecules. These systems were equilibrated by first applying the steepest descent energy minimization algorithm to settle the initial configurations and then using the Nose-Hoover thermostat^{37,38} to raise the average temperature to 300 K. Finally, the density was equilibrated at 1 atm pressure using the Parrinello-Rahman barostat. 39,40

Each production simulation was then run in a constant number/volume/temperature (NVT) canonical ensemble for 2 ns, using a 2 fs time step. Equilibrated box side lengths were 1.663 nm for the pure GC system, 1.665 nm for the system with 27 GC molecules and 1 KF ion pair, and 1.676 nm for the system with the KCl ion pair. Additional classical simulations to test the size dependence were run for the bulk and electrolyte systems where the number of solvent molecules and box side length were increased to 2000 and 6.5 nm, respectively. We saw no significant size dependence in the classical radial distribution functions.

Density functional theory based quantum molecular dynamic simulations were run using the CP2K^{41,42} (v2.6.1) package. The RevPBE/DZVP-MOLOPT-SR-GTH⁴³⁻⁴⁵ functional/basis was used in conjunction with the appropriate RevPBE-optimized GTH pseudopotentials.^{46,47} The D3 dispersion correction with Becke-Johnson damping was included.^{48,49} The initial coordinates for the AIMD simulations were taken from independent equlibrated classical production runs (see Figure 2).

Two simulations contained 32 glycerol carbonate molecules, and simulations of the electrolyte solutions contained 27 glycerol carbonate molecules and one (KF or KCl) ion pair. The starting distances between the ion pairs in the electrolyte systems were chosen to be between 2.8 and 5 Å to allow for the formation of contact or shared-solvent ion pairs during the

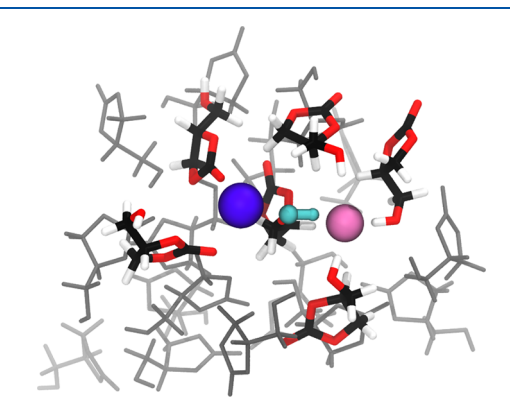


Figure 2. K (purple)—F (pink) ion pair solvated in glycerol carbonate. The first solvation shell is shown in color, and the ion bridging hydroxyl tail is highlighted in cyan. Periodic images have been removed for clarity. Picture generated using AIMD quantum simulation data.

quantum simulations. The ions were restrained to these positions (2.8, 3.2, 3.6, 4.0, and 5.0 Å) during the classical simulations, which followed the same equilibration procedure detailed above. The initial conditions for the AIMD simulations were taken from well-separated configurations along the classical trajectories. These initial configurations were subjected to short energy minimizations carried out via 50-iteration geometry optimizations (using the same RevPBE/DZVP-MOLOPT-SR-GTH functional/basis set) prior to thermal equilibration. A plane-wave integration grid cutoff of 1000 Ry and a relative cutoff of 40 Ry was found to produce minimal errors compared to a benchmark calculation using 2000 and 200 Ry cutoffs.

The PBE functional has been shown to lead to overstructuring in systems with large amounts of hydrogen bonding such as water. ^{50,51} The PBE functional showed a slightly higher degree of hydrogen bonding relative to the RevPBE functional, so the latter was chosen for the final analysis. A 1 fs time step was achieved by transmuting the molecular hydrogens into tritium. ⁵² The production simulations were allowed to first equilibrate for 80 ps, and data were collected for a further 100 ps in the NVT ensemble. AIMD trajectories for comparison with our previous EC and PC simulations were taken from ref 9.

Trajectory analysis was performed using the Trajectory Analyzer and Visualizer program (TRAVIS),⁵³ VMD,⁵⁴ and the GROMACS suite of analysis tools. These codes were utilized to compute radial distribution functions, mean-squared displacements, angular distribution functions, and the viscosity. Radial distribution functions were also converted to potentials of mean force to analyze interaction free energy profiles.

2.2. Charge Transfer Calculations. The charge transfer between associating GC molecules and between GC and ions was analyzed using the ORCA⁵⁵ quantum chemistry program (to calculate electron densities) and a Bader analysis program⁵⁶ (to partition atomic charges). The B3LYP^{57–60} functional in conjunction with the 6-31G** orbital basis set⁶¹ was used to calculate the single-point energies and electron density distributions of 200 dimer conformations. These conformations were taken from the AIMD simulation trajectories. The Bader analysis program was then used to assign charge to each atom center in the simulation, and these results were plotted as histograms for ease of comparison. The Multiwfin program was used to generate the electron density change profiles used to further characterize hydrogen bonds in the systems.⁶² Results from these calculations are summarized in the main text and presented and discussed further in the Supporting Information.

3. RESULTS AND DISCUSSION

3.1. Hydrogen Bonding in Pure Glycerol Carbonate. The hydrogen bonding-type interactions are illustrated via various radial distribution functions (RDFs) in Figure 3 that displays AIMD data for the three carbonate systems (EC, PC, and GC). In the EC system (Figure 3a) the primary interactions

and GC). In the EC system (Figure 3a) the primary interactions are between the carbonyl headgroup (O4) and the hydrogens attached to the bottom of the carbonate ring (highlighted gray in Figure 3). Because of the symmetry of this molecule, the individual profiles for each hydrogen are indistinguishable.

The PC system's profiles (Figure 3b) show that the additional methyl group has little effect on the preference of the carbonyl oxygen for the hydrogens directly attached to the carbonate ring. Even the hydrogen attached to the same carbon as the methyl tail (highlighted in blue) is involved in nearly identical binding to the carbonyl oxygen despite the added excluded volume of the tail itself. This is why the chain-forming liquid structure found in

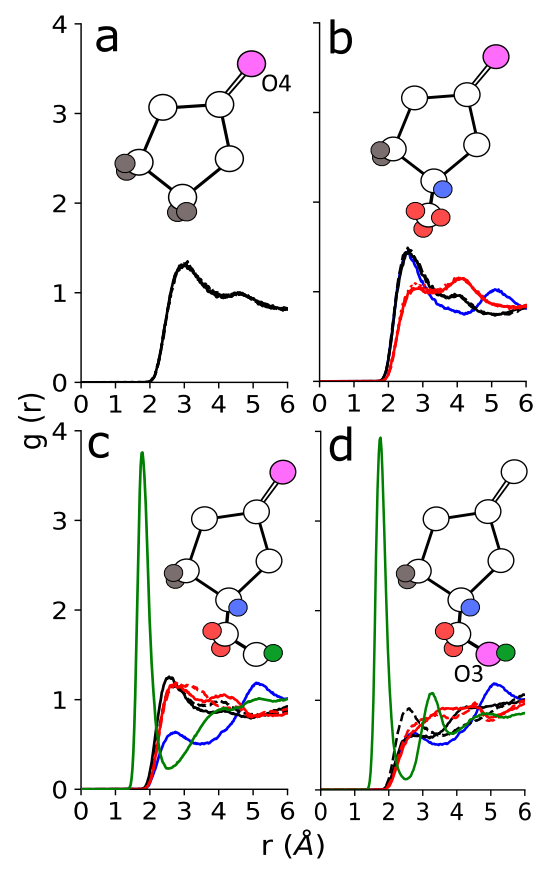


Figure 3. Radial distributions functions describing the association between the oxygens in EC (a), PC (b), and GC (c,d) and the hydrogen bonding sites of neighboring molecules. The highlighted atom colors correspond to profiles of the same color and their interactions with the oxygen (highlighted in pink). All RDFs shown were generated from RevPBE/DZVP-MOLOPT-SR-GTH AIMD data.

EC systems, where the individual molecules line up behind one another facing a common direction, is also present in PC^{23} (see below).

The addition of the OH group in GC promotes hydrogen bonding beyond the weak interactions seen in EC and PC (Figure 3c,d). The dominant RDF features can be seen in the carbonyl's (pink) interaction with the hydrogen of the hydroxyl tail (highlighted green in panel c) and the hydroxyl oxygen's (pink) interaction with other hydroxyl hydrogens (highlighted green in panel d). These new hydrogen bonding interactions are larger in magnitude than other interactions in the GC system and are greater than any interactions seen in the pure EC or PC systems.

There are also differences between GC and EC/PC when examining the carbonyl's interactions with the other hydrogens in the system. For instance, the hydrogen (blue) bound to the branching carbon shows significantly less binding to the carbonyl oxygen in GC. In contrast, the RDFs for the hydrogens bound directly to the ring, but not on the branching carbon, are generally unaffected. This reduction in binding indicates that, not surprisingly, the tail of GC has a larger impact than PC's methyl tail on the local liquid structure. The strength of the hydrogen-bonding interactions results in a reduction in liquid chain-forming ability in GC (see below).

The primary hydrogen bonding interactions in GC that are reported in Figure 3 are compared to the classical results in Figure 4. The potentials of mean force (PMFs) have also been

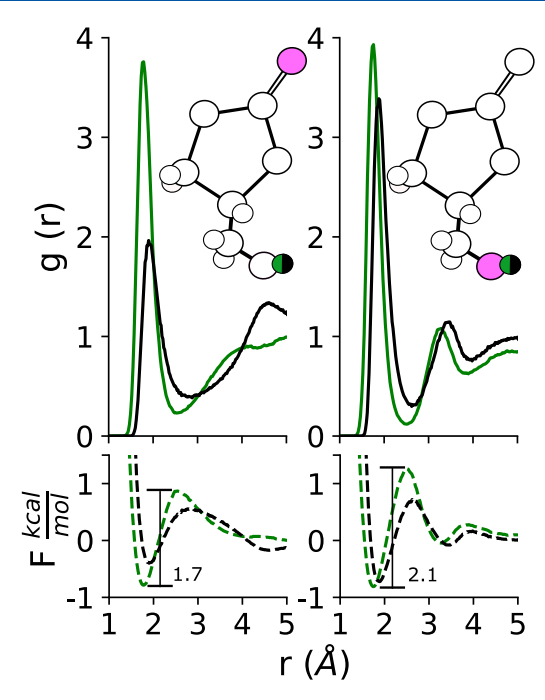


Figure 4. Comparison of classical (black) and AIMD (green) hydrogen bonding RDFs and corresponding potentials of mean force for the pure GC liquid.

calculated from the RDFs. These results show the general underestimation of the hydrogen bonding interactions in the pure GC liquid by the classical model. The potentials of mean force show that the free energy barrier for hydrogen-bond dissociation in the carbonyl-to-hydroxyl interaction is 1.7 kcal/mol and for the hydroxyl-to-hydroxyl interaction is 2.1 kcal/mol in the AIMD simulations. The same interactions in the classical system display free energy barriers to hydrogen bond dissociation of 1.0 and 1.5 kcal/mol, respectively.

The RDFs previously reported for pure GC, based upon the Monte Carlo fit Empirical Potential Structure Refinement (EPSR) method, 23 are even lower in magnitude than those generated here with the OPLS-AA classical model. When other site interaction RDFs are calculated (O4-O4, O4-O1, O4-C2 shown in Figure S1), the differences can be understood as due to the EPSR model's overestimation of the ring-to-ring interactions and underestimation of the carbonyl-to-hydroxyl and/or hydroxyl-to-hydroxyl interactions. This raises the concern of whether the EPSR method for fitting the classical model to the experimental structural data converges to a unique solution for organic solvents with complex interactions. The possible lack of uniqueness is indicated by the ability of our AIMD simulations to replicate the experimental center-of-mass to center-of-mass RDFs and measured structure factors while exhibiting individual pair RDFs that differ substantially from the classical EPSR model

3.2. Dynamics of Pure Glycerol Carbonate. The calculated transport properties of the pure GC liquid are shown in Table 1. Because of the unavailability of a direct experimental measurement of the diffusion coefficient for GC, we have estimated its value using the experimental viscosity and the Stokes–Einstein relation (using a molecular radius of 3 Å, see Figure S2). For reference, the Stokes–Einstein estimate is relatively accurate for water (Stokes–Einstein estimate of 173 Å²/ns versus the experimental value of 298 Å²/ns) and silicon dioxide at high temperature (a highly viscous, glassy system).⁶³

Table 1. Dynamic Quantities of Pure GC at 300 Ka

method	self-diffusion coefficient (\mathring{A}^2/ns)	viscosity (cP)
OPLS-AA	19.6 *	$12.46 \pm 0.9*$
RevPBE	1.4	
experimental	0.89 **	85.00 ¹⁷

**, this work; **, estimated from experimental viscosity via the Stokes-Einstein relation. The classical diffusion constant was calculated as a linear fit of the mean square displacement over the time scale 0.16 to 0.6 ns. The AIMD diffusion constant was computed as a linear fit over the time scale 0.08 to 0.16 ns. The classical and quantum mean square displacement curves are shown in Figure S4.

The classical simulations take advantage of much longer simulation times which allow for computation of the viscosity (using the Berk-Hess particle perturbation method, PPM⁶⁴).

The weaker intermolecular interactions reported in the classical RDFs above lead to poor agreement with experiment for the self-diffusion coefficient and bulk viscosity. These results can be compared with previously reported diffusion calculations for EC and PC. ⁶⁵ The results highlight the added complexity of modeling GC with its prominent hydrogen-bonding interactions.

For comparison, the self-diffusion coefficient calculation based upon the AIMD simulations matches quite well with the experimental estimate (1.4 compared to 0.89 Å $^2/\rm ns$). We note that there is a slight decrease in the slope of the mean square displacement at long times (0.6 to 0.8 ns) in the classical simulation (Figure S4); if the AIMD diffusion constant is correspondingly scaled downward by 20%, the agreement of the computed value with the Stokes–Einstein estimate is quite good. This gives us confidence that the AIMD simulations are faithfully reproducing the structural and dynamic properties of the pure GC system.

3.3. Local Structuring in Pure Glycerol Carbonate. The heatmaps shown in Figures 5 and 6 detail the combined distribution functions (CDFs) which involve the angle between

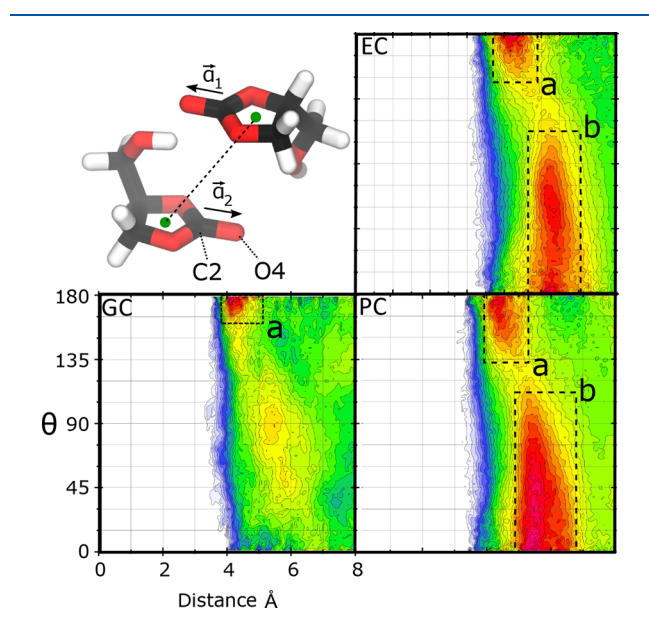


Figure 5. Heatmaps showing chain formation in EC and PC, contrasted with GC. High density regions for all systems are outlined and labeled as "a" or "b". *X*-axis label and ticks for EC/PC are the same as those for GC. Generated using RevPBE/DZVP-MOLOPT-SR-GTH AIMD data.

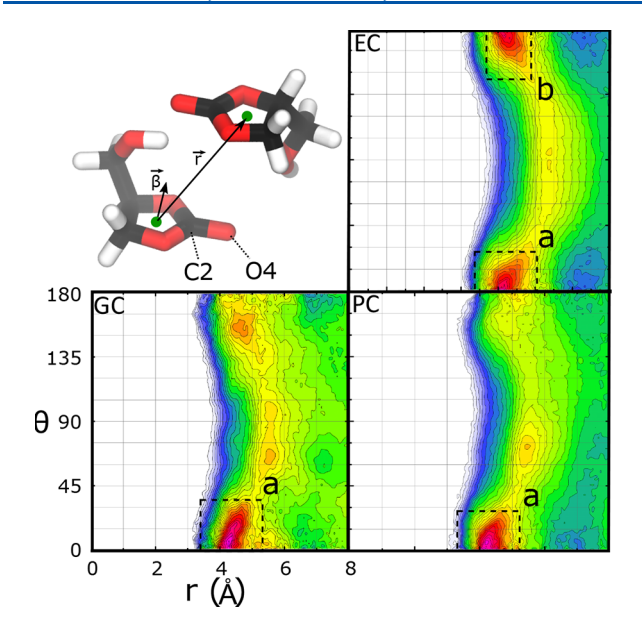


Figure 6. Heatmaps showing molecular stacking formation in EC and PC, contrasted with GC. High density regions for all systems are outlined and labeled as "a" or "b". X-axis label and ticks for EC/PC are the same as those for GC. Generated using RevPBE/DZVP-MOLOPT-SR-GTH AIMD data.

two defined vectors and the distance between the molecule center-of-masses to which the vectors belong. These CDFs allow us to probe the extent of specific structural modes commonly found in carbonate systems.

The first mode is molecular chain formation. As described above, molecules that undergo chain formation line up one behind another with their dipoles pointing in the same direction. In the case of EC and PC, this means that the carbonyl bonds point in the same direction (see Figure S3 for schematic structures). We can measure the degree to which two molecule's dipoles line up by defining a vector along that dipole (the carbonyl bond in EC, PC, and GC) and measuring the angle between that vector and the same vector on a neighboring molecule. The defined vectors are displayed in the Figure 5 inset image and are labeled \vec{a} . Each heatmap compares GC's structure with that of EC and PC.

In Figure 5, the first region of interest ("a") shows the density for molecules interacting at a close range of 4-5 Å. All three systems display high density at this distance peaking near 180° . This means that two carbonate molecules interacting most closely strongly prefer to have their carbonyl groups pointing in opposite directions. This is consistent with a stacking arrangement and will be further explored when combined with the results in Figure 6.

The second region in Figure 5 ("b") is where we see the differences between GC and the other carbonates. In this region, molecules that are far enough away to be directly behind or in front of the reference molecule show high density near 0° if chain formation occurs. In contrast with the other carbonates, GC shows no high density in this area and therefore there is no sign of chain formation in its liquid phase. The "b" regions for EC and PC are spread out more than their "a" regions due to the flexible nature of the molecular chains. This gives a wider range of angles for which they can still be said to be associating.

The second CDF displayed in Figure 6 gives insight into the extent and nature of molecular stacking in each system. Similar to the previous heatmap, two vectors are defined, but in this case

they are not identical. The first is the vector normal to the GC molecule's ring (labeled as $\vec{\beta}$) and the second is drawn along the line connecting the reference GC molecule's ring center to a neighboring GC's ring center (labeled as \vec{r}). This angle, when combined with the distance, allows for pinning down the position of the closely interacting, opposite facing molecules that were shown to be present in the "a" density areas in Figure 5.

Taking the EC system as a reference (Figure S3), stacking occurs when one molecule sits on top of another and is predominantly accompanied by the carbonyl bonds pointing in opposite directions. If there is the ability for more than one molecule to associate with the reference, then there will be two regions of high density, and that is what we see for EC. The density labeled "a" shows that one EC molecule is stacking on the bottom of the reference EC, and the density hot spot labeled "b" shows that another molecule associates from the top as well. This indicates the potential of EC to form long-range structuring in the direction perpendicular to the chain formation direction.

The above bidirectional stacking observed in EC is missing in the GC and PC systems that display stacking in one direction only. The fact that we see density only near 0° for GC and PC means that in order to stack both molecules have to be facing one another. That is to say, their tails are pointing toward the other molecule to which it associates. In GC, this allows for the relatively strong binding of each molecule's carbonyl group to the other's hydroxyl tail.

The liquid structure in GC is mediated by the previously described hydrogen bonding in the system. The bonding between the carbonyl group and the hydroxyl hydrogen can lead to an orientation-specific stacking conformation where two GC molecules are bound facing one another. On the other hand, the hydrogen bonding between the hydroxyl tails of neighboring GC molecules again leads to dimer formation, but these dimers are observed to move more freely relative to each other (being bound only by their tails). The competition between these sites and the blocking of chain formation by the tail of GC leads to a more disordered liquid²³ relative to both EC and PC. Even though the GC liquid is more disordered, the relatively strong hydrogen bonding of the pairs results in a much higher viscosity relative to EC and PC.

3.4. Structure in GC Electrolyte Solutions. The natural next step after examining the pure GC solutions is to extend our investigation to the physical properties of the GC electrolyte solutions. The ion pairs chosen are KF and KCl, which have been experimentally examined in refs 10 and 22. Dissolved KF produces a significant shift in $T_{\rm g}$ while KCl does not. These systems were modeled with both classical and AIMD methods. The classical simulations were used to probe a variety of concentrations for the electrolytes, whereas the AIMD simulations were limited to one concentration and were used to evaluate the performance of the classical model.

Sarri et al. ^{10,22} hypothesized that the interaction responsible for the glass transition temperature increase seen in the KF solution but not in the KCl solution is the stronger hydrogen bonding of the GC tail to the F⁻ ion relative to the Cl⁻ ion. The RDFs in Figure 7 detail these interactions for the KF system. As can be seen in both the classical and AIMD simulations, the interactions are significant with both classical and quantum models predicting strong binding of the hydroxyl hydrogen with the fluoride ion. The classical model overestimates the interactions, compared to the AIMD simulations, at both low and high concentrations. These results can be contrasted with those above for the pure GC liquid, where hydrogen bonding is

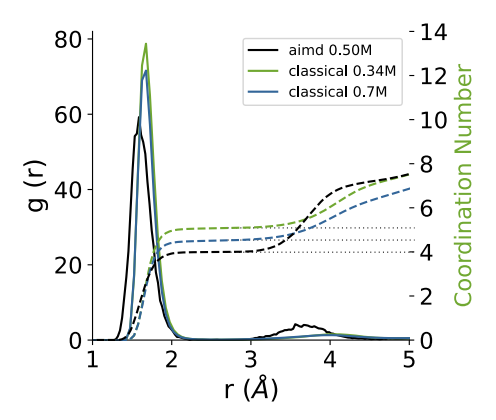


Figure 7. RDFs describing the binding of GC to fluoride through the hydrogen of the hydroxyl tail in the KF electrolyte solutions. Classical (blue and green) and AIMD (black).

underestimated by the classical model. Thus, a uniform charge scaling approach is likely to encounter difficulties in modeling the diverse behaviors observed in GC.

To investigate these issues, we scaled²⁷ our GC partial charges to 110, 90, 80, and 70% of their original values. Even with this scaling (that proved helpful for studies of the EC and PC solutions²⁷), the classical models failed to match the anion binding distance and magnitude seen in our AIMD simulations (corresponding RDFs, Figures S5–S8).

The classical model's overestimation of the anion/GC binding leads to 5 GC molecules associated with the F⁻ ion at high concentrations, larger than our AIMD-predicted coordination number of 4. The fourth GC bound to the fluoride ion serves a key role in this system as a shared-solvent bridge between the F⁻ and K⁺ ions. This bridging GC molecule inserts its tail to stabilize KF as a shared-solvent ion pair (see Figure 2 above and results below) instead of contact ion pairs, triplet, or free ions as seen in the more extensive classical simulations. Another interesting and important difference between the AIMD and classical simulations appears in the 3–4 Å range in the ion/solvent RDFs. In that region, the AIMD simulations suggest a second solvation shell that includes three additional GCs

The differences in ion pairing described above are quantified in the cation—anion RDFs in Figure 8. These RDFs show that the shared-solvent ion pair is unique to the AIMD KF simulations, as evidenced by a peak in the 4–5.5 Å range.

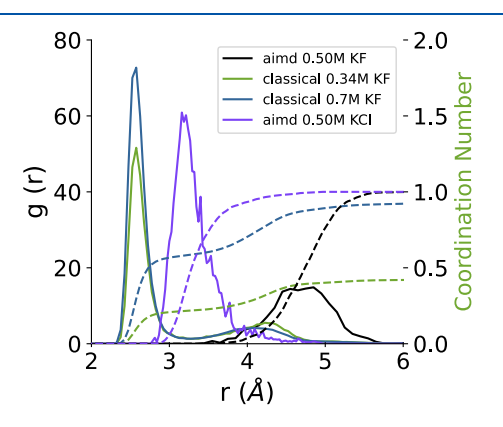


Figure 8. Comparison of AIMD ion association in KF (black)/KCl solutions (purple), and the impact of electrolyte concentration on classical representations (blue and green).

This shared-solvent ion pair structure forms within 20 ps in each of the AIMD KF simulations regardless of initial starting position. In addition, the shared-solvent ion pair remains stable for at least 180 ps. The classically modeled KF prefers a contact ion pair configuration. For the KCl ion pair, on the other hand, the AIMD simulations produce a contact ion pair (as does the classical model).

To continue the investigation of the differences in solvent interactions between the KF and KCl electrolytes, RDFs have been calculated to investigate the hydrogen bonding experienced by the anion in both systems. We also examined the changes in binding between the potassium ion and the oxygens of GC. The strong hydrogen bonding between the hydroxyl hydrogen and the anion found in KF is reduced in KCl. This is illustrated in the PMFs which reveal a reduction in the free energy barrier to ion pair dissociation from 5.5 to 3.1 kcal/mol (Figure 9).

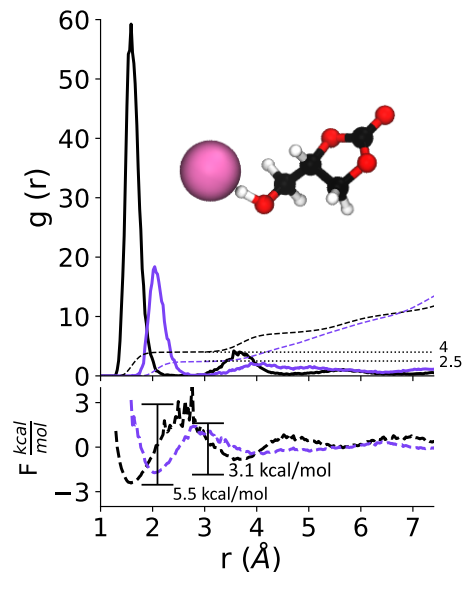


Figure 9. RDFs describing the binding of H6 to fluoride (black) and chloride (purple), both with potassium present in the system. Calculated from AIMD simulation data.

In the first solvation shell, the Cl $^-$ anion binds 2.5 GC molecules on average compared to 4 for fluoride. The second solvation shells around the anion also differ significantly in KCl relative to KF. In the 3–4 Å range of Figure 9, the KF system gains 3 GC molecules, whereas the chloride anion only gains 1–2 GC molecules. This displays the ion specific structuring unique to each anion, with the F $^-$ anion displaying significantly more induced structure relative to Cl $^-$. This observation is likely involved in the significant increase in $T_{\rm g}$ for the KF solution with little change for the KCl solution.

The cation interactions with oxygens in the KCl system are similar to those in KF (Figure 10 left), but there is a reduction in the binding of the K^+ ion with O3 that can be traced to the bridging GC molecule no longer being locked in between the ions (Figure 10, right side).

The change from shared-solvent (KF) to contact (KCl) ion pair structures also affects the geometry of GC molecules around the anions. The distributions of the angle determined by the GC-ligand to fluoride to GC-ligand angle are displayed in Figure 11. From the distribution of this angle, we see that there is a preference for tetrahedral geometry in the first solvation shell of

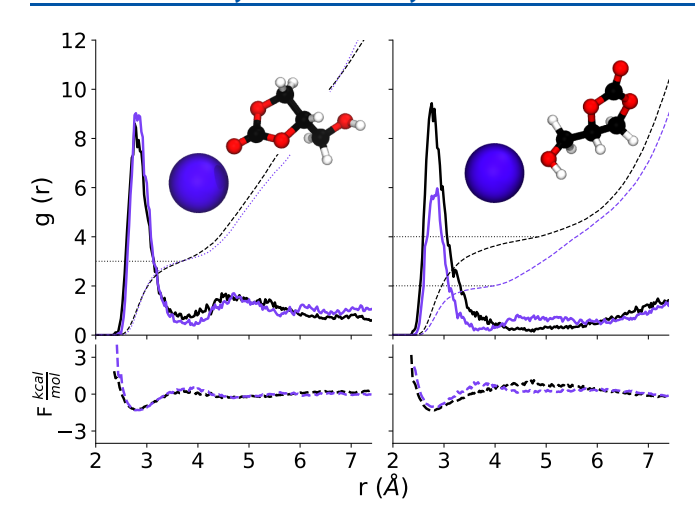


Figure 10. RDFs describing the binding of O4 (left) and O3 (right) to potassium in KF (black) and KCl (purple) electrolyte systems. Calculated from AIMD simulation data.

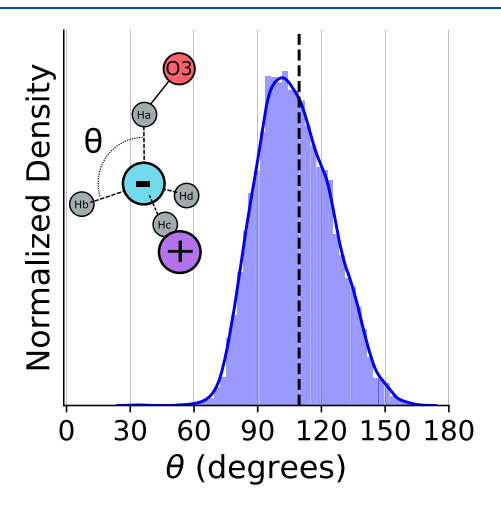


Figure 11. Distribution of the ligand—anion—ligand angle that describe the first shell geometry around the fluoride anion.

fluoride in the KF system. In an ideal system, this would manifest as a distribution centered at 109.5°, but the presence of the potassium ion appears to shift this peak of the distribution slightly downward. This could be due to the potassium ion squeezing the interacting GC molecules closer together toward the side opposite the cation.

For the KCl system (Figure 12), we see a mixture of solvation structures. The most commonly occurring consists of 2 GC molecules and the binding potassium. These three ligands form a shifted trigonal-planar geometry where the ligand—anion—ligand angle (which in an ideal system would be 120°) can be broken into two separate distributions. The first distribution centered at 89.5° follows the angle between the two associating GC molecules. The second, centered near 125° , follows the angle between each of the associating GC molecules and the potassium ion. These angles can be seen in the inset image in Figure 12 labeled as θ_1 and θ_2 , respectively.

We suggest two factors are driving the distributions away from the ideal trigonal planar value of 120°. First, as evidenced in Figure 9 above, there is a third GC molecule that can enter the first solvation shell of the chloride ion. This influence would shift the two ligand—anion—ligand angles we have observed downward. Second, the potassium ion, as a large positively charged

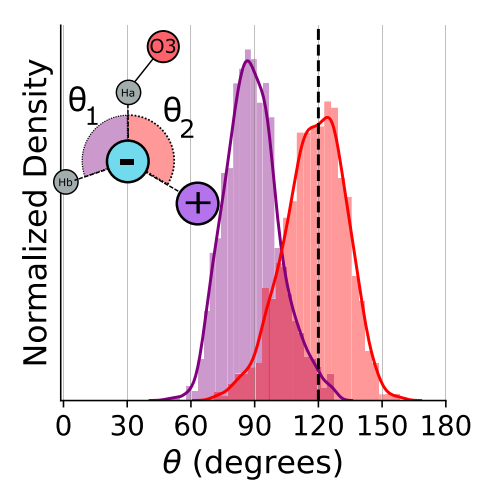


Figure 12. Distributions of the ligand—anion—ligand angles that describe the first shell geometry around the chloride anion.

species, can push the associating GC ligands away from itself. This would cause them to group together on the opposite side of the anion, shifting their association angle downward while shifting the second angle we measured, θ_2 , slightly higher. This explains why the GC-anion-GC angle (θ_1) is shifted lower while the GC-anion-potassium angle stays close to 120° .

3.5. Charge Transfer in GC Electrolyte Solution. Both hydrogen bonds between nearby GC molecules and interactions of ions with their solvation shells involve strong forces that can display chemical character. Results pertaining to charge transfer (CT) in these two bonding modes are presented in the Supporting Information (Figures S9–S13 and Table 1). The configurations for the calculations were taken from the AIMD simulations. Charge density distributions are presented along with data using the Bader charge partitioning method.

For the GC-GC hydrogen bonds, there is clear polarization in both the hydroxyl/carbonyl and hydroxyl/hydroxyl interactions (Figure S9). The electron density around the H-bonding hydrogens on the hydroxyl groups is depleted, while there is a buildup of electron density on the oxygens to which the hydrogens bond (Figure S10). The charge redistribution pattern is complex with a multipolar character. In order for a polarizable model to accurately capture the charge redistributions and resulting interactions, it is likely that multiple distributed polarizable sites (Drude or point dipole) would thus be necessary. Since these hydrogen bonds are crucial for determining the physical properties of the GC solutions, it is clear that classical models should be guided by data from the quantum simulations.

The ion/GC interactions also display chemical complexity (Figures S11–S13 and Table 1). For these calculations, the individual ions were simulated in the GC liquid without counterions. Comparing charge transfer between the F⁻ and Cl⁻ ions and GC, they both lose approximately 0.2e as electron density spills out onto the surrounding solvent molecules. There appears to be a balance between the "harder" nature of the F⁻ ion with its stronger electric field and more chemical-type interactions with the GC hydroxyl tail. In contrast, the "softer" Cl⁻ ion is more polarizable and displays less intimate chemical interactions with GC. The net result is a comparable level of CT from the anions to the GC solvent. The total binding of the fluoride ion through an H-bond to the GC molecule is significantly stronger than that of the chloride ion. On the

other hand, the net CT from the solvent to the K^+ cation is roughly 0.1e or half that observed for the anions.

4. CONCLUSIONS

The aim of this paper has been to gain initial insights into local molecular structure and dynamics in glycerol carbonate (GC) electrolyte solutions via quantum and classical molecular dynamics simulations. The work was motivated by recent experiments highlighting the interesting physical behaviors of the cyclic carbonate sequence EC/PC/GC. ^{6,7,10,22,23} An interesting further goal is to compare and contrast ion solvation in these organic liquids with hydration in water. ⁶⁶ The cyclic carbonate molecules have larger dipoles and polarizabilities than water, but similar dielectric constants. They thus serve as effective solvents for ions, for example, in lithium-ion batteries. The present study examines the properties of the pure GC liquid and the solvation of the KF and KCl ion pairs in GC.

In terms of pure GC properties, the quantum AIMD simulations reveal the important role of hydrogen bonding in determining the structural and dynamical properties of the liquid. Accurate representation of the molecular interactions is clearly required to reproduce the transport properties: the diffusion constant is overestimated by a factor of 22 with the OPLS-AA classical point charge model, while the quantum AIMD simulations produce relatively good agreement with experiment. The classically computed viscosity is correspondingly lower than the experimental value. The AIMD simulations also accurately reproduce the measured structure factor of GC. ²³

Further analysis of the average structure of the EC/PC/GC sequence reveals differing structural motifs for each liquid. EC exhibits formation of molecular chains and stacking both above and below a chosen molecular plane, PC shows some chain formation but dimer formation rather than bidirectional stacking, and GC displays no chain formation and the formation of more strongly bound dimers due to hydrogen bonding. In this sense, the GC liquid is the most disordered of the three cyclic carbonates (lacking longer-ranged order), in agreement with the neutron scattering results.²³ The strong interactions involved in the extensive hydrogen bonding produce the high viscosity of GC relative to EC, PC, and water.

The addition of the KF and KCl ion pairs allows for a detailed analysis of local structure involved in specific-ion solvation in the complex GC liquid. For the KF electrolyte, the classical simulations predict a contact ion pair, while the quantum simulations display a shared-solvent ion pair in which the OH group from GC inserts between the ions. This structural pattern was observed in several AIMD simulations that started with initial ion configurations ranging from direct contact to distances nearly those seen in the shared-solvent geometry. The shared-solvent structure likely is involved with the observed increase in viscosity upon addition of KF to pure GC, along with the increased glass transition temperature. ¹⁰ In addition, the classical model overestimates direct hydrogen bonding between GC and the anion.

The KCl pair, on the other hand, displays a contact ion pair configuration in both classical and quantum simulations. The hydrogen bonding is clearly weaker for the interaction of the OH group of GC with the Cl $^-$ ion (relative to F $^-$). These results support the hypothesis from ref 22 that the strong interactions of GC with the F $^-$ ion are central to the observed macroscopic properties such as higher glass transition temperature and solution viscosity.

The observation that the classical models underestimate hydrogen bonding in pure GC while overestimating the hydrogen bonding of GC with the anions reveals the complexity of the interactions involved in this molecular liquid. Thus, quantum AIMD simulations can provide benchmark results on local structure and dynamics that lead to the development of more accurate classical models. Classical models are required for the simulation of larger-scale phenomena such as phase transitions and viscosities. A future goal is to develop such classical models that capture the essential interactions in solvation.

ASSOCIATED CONTENT

Supporting Information

The Supporting Information is available free of charge at https://pubs.acs.org/doi/10.1021/acs.jpcb.0c10942.

Radial distribution functions for glycerol carbonate, structure factors, schematic diagram of liquid structural motifs, mean-square displacements, structural results from scaled-charge simulations, data from charge transfer calculations (PDF)

AUTHOR INFORMATION

Corresponding Authors

Andrew E. Eisenhart — Department of Chemistry, University of Cincinnati, Cincinnati, Ohio 45221, United States; Email: eisenhaw@mail.uc.edu

Thomas L. Beck — Department of Chemistry, University of Cincinnati, Cincinnati, Ohio 45221, United States;
orcid.org/0000-0001-8973-7145; Email: becktl@ucmail.uc.edu

Complete contact information is available at: https://pubs.acs.org/10.1021/acs.jpcb.0c10942

Notes

The authors declare no competing financial interest.

ACKNOWLEDGMENTS

We thank Pierandra Lo Nostro and Barry Ninham for helpful discussions. We are grateful for the numerous contributions of Lawrence Pratt to our work on ion solvation in molecular liquids. This material is based upon work supported by the National Science Foundation under Grants CHE-1565632 and CHE-1955161. The computations were performed at the Ohio Supercomputer Center and the University of Cincinnati Advanced Research Computing Center.

REFERENCES

- (1) Goodenough, J. B.; Park, K.-S. The Li-Ion Rechargeable Battery: a Perspective. *J. Am. Chem. Soc.* **2013**, *135*, 1167–1176.
- (2) Melot, B. C.; Tarascon, J.-M. Design and Preparation of Materials for Advanced Electrochemical Storage. *Acc. Chem. Res.* **2013**, *46*, 1226–1238.
- (3) Choi, N.-S.; Chen, Z.; Freunberger, S. A.; Ji, X.; Sun, Y.-K.; Amine, K.; Yushin, G.; Nazar, L. F.; Cho, J.; Bruce, P. G. Challenges Facing Lithium Batteries and Electrical Double-Layer Capacitors. *Angew. Chem., Int. Ed.* **2012**, *51*, 9994–10024.
- (4) Xu, K. Electrolytes and Interphases in Li-Ion Batteries and Beyond. *Chem. Rev.* **2014**, *114*, 11503–11618.
- (5) Xu, K. Nonaqueous Liquid Electrolytes for Lithium-Based Rechargeable Batteries. Chem. Rev. 2004, 104, 4303—4418.

- (6) Peruzzi, N.; Ninham, B. W.; Lo Nostro, P.; Baglioni, P. Hofmeister Phenomena in Nonaqueous Media: The Solubility of Electrolytes in Ethylene Carbonate. J. Phys. Chem. B 2012, 116, 14398-14405.
- (7) Peruzzi, N.; Lo Nostro, P.; Ninham, B. W.; Baglioni, P. The Solvation of Anions in Propylene Carbonate. J. Solution Chem. 2015, 44, 1224-1239.
- (8) Chernyak, Y. Dielectric Constant, Dipole Moment, and Solubility Parameters of Some Cyclic Acid Esters. J. Chem. Eng. Data 2006, 51,
- (9) Pollard, T. P.: Beck, T. L. Structure and Polarization Near the Li+ Ion in Ethylene and Propylene Carbonates. J. Chem. Phys. 2017, 147,
- (10) Sarri, F.; Tatini, D.; Tanini, D.; Simonelli, M.; Ambrosi, M.; Ninham, B. W.; Capperucci, A.; Dei, L.; Lo Nostro, P. Specific Ion Effects in Non-Aqueous Solvents: The Case of Glycerol Carbonate. J. Mol. Lig. 2018, 266, 711-717.
- (11) Behr, A.; Eilting, J.; Irawadi, K.; Leschinski, J.; Lindner, F. Improved Utilisation of Renewable Resources: New Important Derivatives of Glycerol. Green Chem. 2008, 10, 13-30.
- (12) Rousseau, J.; Rousseau, C.; Lynikaite, B.; Šačkus, A.; de Leon, C.; Rollin, P.; Tatibouët, A. Tosylated Glycerol Carbonate, a Versatile Biselectrophile to Access new Functionalized Glycidol Derivatives. Tetrahedron 2009, 65, 8571-8581.
- (13) Corma, A.; Iborra, S.; Velty, A. Chemical Routes for the Transformation of Biomass into Chemicals. Chem. Rev. 2007, 107, 2411-2502.
- (14) Zheng, Y.; Chen, X.; Shen, Y. Commodity Chemicals Derived from Glycerol, an Important Biorefinery Feedstock. Chem. Rev. 2010, 110, 1807.
- (15) Werpy, T.; Petersen, G. Top Value Added Chemicals from Biomass: Vol. I - Results of Screening for Potential Candidates from Sugars and Synthesis Gas; National Renewable Energy Laboratory Website; https://www.nrel.gov/docs/fy04osti/35523.pdf (accessed Feb. 3, 2021).
- (16) Schaffner, B.; Schaffner, F.; Verevkin, S. P.; Borner, A. Organic Carbonates as Solvents in Synthesis and Catalysis. Chem. Rev. 2010, 110, 4554-4581.
- (17) Sonnati, M. O.; Amigoni, S.; de Givenchy, E. P. T.; Darmanin, T.; Choulet, O.; Guittard, F. Glycerol Carbonate as a Versatile Building Block for Tomorrow: Synthesis, Reactivity, Properties and Applications. Green Chem. 2013, 15, 283-306.
- (18) Seong, P.-J.; Jeon, B. W.; Lee, M.; Cho, D. H.; Kim, D.-K.; Jung, K. S.; Kim, S. W.; Han, S. O.; Kim, Y. H.; Park, C. Enzymatic Coproduction of Biodiesel and Glycerol Carbonate from Soybean Oil and Dimethyl Carbonate. Enzyme Microb. Technol. 2011, 48, 505-509.
- (19) Ou, G.; He, B.; Li, X.; Lei, J. Glycerol Carbonate: a Novel Biosolvent with Strong Ionizing and Dissociating powers. Sci. World J. 2012, 2012, 1.
- (20) Dei, L.; Grassi, S. Peculiar Properties of Water as Solute. J. Phys. Chem. B 2006, 110, 12191-12197.
- (21) Chaudhari, M. I.; Vanegas, J. M.; Pratt, L. R.; Muralidharan, A.; Rempe, S. B. Hydration Mimicry by Membrane Ion Channels. Annu. Rev. Phys. Chem. 2020, 71, 461-484.
- (22) Sarri, F.; Tatini, D.; Ambrosi, M.; Carretti, E.; Ninham, B. W.; Dei, L.; Lo Nostro, P. The Curious Effect of Potassium Fluoride on Glycerol Carbonate. How Salts Can Influence the Structuredness of Organic Solvents. J. Mol. Liq. 2018, 255, 397-405.
- (23) Delavoux, Y. M.; Gilmore, M.; Atkins, M. P.; Swadźba-Kwaśny, M.; Holbrey, J. D. Intermolecular Structure and Hydrogen-Bonding in Liquid 1, 2-Propylene Carbonate and 1, 2-Glycerol Carbonate Determined by Neutron Scattering. Phys. Chem. Chem. Phys. 2017, 19, 2867-2876.
- (24) Lamoureux, G.; Roux, B. Absolute Hydration Free Energy Scale for Alkali and Halide Ions Established from Simulations with a Polarizable Force Field. J. Phys. Chem. B 2006, 110, 3308-3322.
- (25) Lopes, P. E.; Roux, B.; MacKerell, A. D. Molecular Modeling and Dynamics Studies with Explicit Inclusion of Electronic Polarizability: Theory and Applications. Theor. Chem. Acc. 2009, 124, 11-28.

I

- (26) Bedrov, D.; Piquemal, J.-P.; Borodin, O.; MacKerell, A. D., Jr; Roux, B.; Schröder, C. Molecular Dynamics Simulations of Ionic Liquids and Electrolytes Using Polarizable Force Fields. Chem. Rev. 2019, 119, 7940-7995.
- (27) Chaudhari, M. I.; Nair, J. R.; Pratt, L. R.; Soto, F. A.; Balbuena, P. B.; Rempe, S. B. Scaling Atomic Partial Charges of Carbonate Solvents for Lithium Ion Solvation and Diffusion. J. Chem. Theory Comput. 2016, 12, 5709-5718.
- (28) Cui, K.; Yethiraj, A.; Schmidt, J. R. Influence of Charge Scaling on the Solvation Properties of Ionic Liquid Solutions. J. Phys. Chem. B 2019, 123, 9222-9229.
- (29) Arslanargin, A.; Powers, A.; Beck, T. L.; Rick, S. W. Models of Ion Solvation Thermodynamics in Ethylene Carbonate and Propylene Carbonate. J. Phys. Chem. B 2016, 120, 1497-1508.
- (30) Ganesh, P.; Jiang, D.-e.; Kent, P. Accurate Static and Dynamic Properties of Liquid Electrolytes for Li-Ion Batteries from Ab Initio Molecular Dynamics. J. Phys. Chem. B 2011, 115, 3085-3090.
- (31) Barnes, T. A.; Kaminski, J. W.; Borodin, O.; Miller, T. F., III Ab Initio Characterization of the Electrochemical Stability and Solvation Properties of Condensed-phase Ethylene Carbonate and Dimethyl Carbonate Mixtures. J. Phys. Chem. C 2015, 119, 3865-3880.
- (32) Abraham, M. J.; Murtola, T.; Schulz, R.; Páll, S.; Smith, J. C.; Hess, B.; Lindahl, E. GROMACS: High Performance Molecular Simulations Through Multi-Level Parallelism from Laptops to Supercomputers. SoftwareX 2015, 1, 19-25.
- (33) Jorgensen, W. L.; Tirado-Rives, J. Potential Energy Functions for Atomic-Level Simulations of Water and Organic and Biomolecular Systems. Proc. Natl. Acad. Sci. U. S. A. 2005, 102, 6665-6670.
- (34) Dodda, L. S.; Vilseck, J. Z.; Tirado-Rives, J.; Jorgensen, W. L. 1.14* CM1A-LBCC: Localized Bond-Charge Corrected CM1A Charges for Condensed-Phase Simulations. J. Phys. Chem. B 2017, 121, 3864-3870.
- (35) Dodda, L. S.; Cabeza de Vaca, I.; Tirado-Rives, J.; Jorgensen, W. L. LigParGen Web Server: an Automatic OPLS-AA Parameter Generator for Organic Ligands. Nucleic Acids Res. 2017, 45, W331-
- (36) Essmann, U.; Perera, L.; Berkowitz, M. L.; Darden, T.; Lee, H.; Pedersen, L. G. A Smooth Particle Mesh Ewald Method. J. Chem. Phys. 1995, 103, 8577-8593.
- (37) Nosé, S. A Molecular Dynamics Method for Simulations in the Canonical Ensemble. Mol. Phys. 1984, 52, 255-268.
- (38) Hoover, W. G. Canonical Dynamics: Equilibrium Phase-Space Distributions. Phys. Rev. A: At., Mol., Opt. Phys. 1985, 31, 1695.
- (39) Parrinello, M.; Rahman, A. Polymorphic Transitions in Single Crystals: A New Molecular Dynamics Method. J. Appl. Phys. 1981, 52, 7182-7190.
- (40) Nosé, S.; Klein, M. Constant Pressure Molecular Dynamics for Molecular Systems. Mol. Phys. 1983, 50, 1055-1076.
- (41) Borštnik, U.; Van de Vondele, J.; Weber, V.; Hutter, J. Sparse Matrix Multiplication: The Distributed Block-Compressed Sparse Row Library. Parallel Comput 2014, 40, 47-58.
- (42) Hutter, J.; Iannuzzi, M.; Schiffmann, F.; Van de Vondele, J. Cp2k: Atomistic Simulations of Condensed Matter Systems. Wiley Interdiscip. Rev. Comput. Mol. Sci. 2014, 4, 15-25.
- (43) Van de Vondele, J.; Hutter, J. Gaussian Basis Sets for Accurate Calculations on Molecular Systems in Gas and Condensed Phases. J. Chem. Phys. 2007, 127, 114105.
- (44) Krack, M. Pseudopotentials for H to Kr Optimized for Gradient-Corrected Exchange-Correlation Functionals. Theor. Chem. Acc. 2005, 114, 145-152.
- (45) Perdew, J. P.; Burke, K.; Ernzerhof, M. Generalized Gradient Approximation Made Simple. Phys. Rev. Lett. 1996, 77, 3865.
- (46) Hartwigsen, C.; Gœdecker, S.; Hutter, J. Relativistic Separable Dual-Space Gaussian Pseudopotentials from H to Rn. Phys. Rev. B: Condens. Matter Mater. Phys. 1998, 58, 3641.
- (47) Goedecker, S.; Teter, M.; Hutter, J. Separable Dual-Space Gaussian Pseudopotentials. Phys. Rev. B: Condens. Matter Mater. Phys. 1996, 54, 1703.

- (48) Grimme, S.; Ehrlich, S.; Goerigk, L. Effect of the Damping Function in Dispersion Corrected Density Functional Theory. *J. Comput. Chem.* **2011**, 32, 1456–1465.
- (49) Grimme, S.; Antony, J.; Ehrlich, S.; Krieg, H. A Consistent and Accurate Ab Initio Parametrization of Density Functional Dispersion Correction (DFT-D) for the 94 Elements H-Pu. *J. Chem. Phys.* **2010**, 132, 154104.
- (50) Bankura, A.; Karmakar, A.; Carnevale, V.; Chandra, A.; Klein, M. L. Structure, Dynamics, and Spectral Diffusion of Water from First-Principles Molecular Dynamics. *J. Phys. Chem. C* **2014**, *118*, 29401–20411
- (51) Forster-Tonigold, K.; Groß, A. Dispersion Corrected RPBE Studies of Liquid Water. J. Chem. Phys. 2014, 141, 064501.
- (52) Leung, K.; Budzien, J. L. Ab Initio Molecular Dynamics Simulations of the Initial Stages of Solid-Electrolyte Interphase Formation on Lithium Ion Battery Graphitic Anodes. *Phys. Chem. Chem. Phys.* **2010**, *12*, 6583–6586.
- (53) Brehm, M.; Kirchner, B. TRAVIS a Free Analyzer and Visualizer for Monte Carlo and Molecular Dynamics Trajectories. *J. Chem. Inf. Model.* **2011**, *51*, 2007–2023.
- (54) Humphrey, W.; Dalke, A.; Schulten, K. VMD: Visual Molecular Dynamics. *J. Mol. Graphics* **1996**, *14*, 33–38.
- (55) Neese, F. The ORCA Program System. Wiley Interdiscip. Rev.: Comput. Mol. Sci. 2012, 2, 73–78.
- (56) Tang, W.; Sanville, E.; Henkelman, G. A Grid-Based Bader Analysis Algorithm Without Lattice Bias. *J. Phys.: Condens. Matter* **2009**, 21, 084204.
- (57) Becke, A. D. Density-Functional Thermochemistry. III. The Role of Exact Exchange. *J. Chem. Phys.* **1993**, *98*, 5648–5652.
- (58) Lee, C.; Yang, W.; Parr, R. G. Development of the Colle-Salvetti Correlation-Energy Formula into a Functional of the Electron Density. *Phys. Rev. B: Condens. Matter Mater. Phys.* **1988**, *37*, 785.
- (59) Vosko, S. H.; Wilk, L.; Nusair, M. Accurate Spin-Dependent Electron Liquid Correlation Energies for Local Spin Density Calculations: a Critical Analysis. *Can. J. Phys.* **1980**, *58*, 1200–1211.
- (60) Stephens, P.; Devlin, F.; Chabalowski, C.; Frisch, M. J. Ab Initio Calculation of Vibrational Absorption and Circular Dichroism Spectra Using Density Functional Force Fields. *J. Phys. Chem.* **1994**, 98, 11623–11627
- (61) Hehre, W. J.; Ditchfield, R.; Pople, J. A. Self—Consistent Molecular Orbital Methods. XII. Further Extensions of Gaussian—Type Basis Sets for use in Molecular Orbital Studies of Organic Molecules. *J. Chem. Phys.* **1972**, *56*, 2257–2261.
- (62) Lu, T.; Chen, F. Multiwfn: a Multifunctional Wavefunction Analyzer. J. Comput. Chem. 2012, 33, 580-592.
- (63) Avramov, I. Relationship between diffusion, self-diffusion and viscosity. J. Non-Cryst. Solids 2009, 355, 745–747.
- (64) Hess, B. Determining the Shear Viscosity of Model Liquids from Molecular Dynamics Simulations. *J. Chem. Phys.* **2002**, *116*, 209–217.
- (65) You, X.; Chaudhari, M. I.; Rempe, S. B.; Pratt, L. R. Dielectric Relaxation of Ethylene Carbonate and Propylene Carbonate from Molecular Dynamics Simulations. *J. Phys. Chem. B* **2016**, *120*, 1849–1853
- (66) Pollard, T. P.; Beck, T. L. Toward a Quantitative Theory of Hofmeister Phenomena: From Quantum Effects to Thermodynamics. *Curr. Opin. Colloid Interface Sci.* **2016**, 23, 110–118.